CONTENT-AWARE NEURON IMAGE ENHANCEMENT

Haoyi Liang, Scott T. Acton and Daniel S. Weller

University of Virginia, Department of ECE, Charlottesville, VA, 22904, USA

ABSTRACT

Neuron microscopy enables advances in the exploration of neural anatomy and function, and neuron image enhancement is typically necessary before higher-level analyses. Most existing neuron image enhancement methods exploit the unique tubular structure of neurons. However, such methods do not preserve neuron details. In this paper, we propose a content-aware neuron image enhancement (CaNE) method that combines the neuron image properties of gradient sparsity and tubular structure. Experiments show that neuron images enhanced by CaNE possess 20% more details in terms of correlation as compared to existing methods. With high-quality neuron images provided by CaNE, neuron analyses, such as segmentation and skeleton detection, are enabled at higher rates of success as described in this paper.

Index Terms—Neuron image, enhancement, gradient sparsity, tubular structure

1. INTRODUCTION

Optical microscopy provides an intuitive way to visualize the structure of neurons. As much neuroscience literature points out, neuron structures provide important clues about the functionality of neurons [1–3]. However, due to the microscopic scale, neuron imaging suffers from numerous distortions, such as noise, clutter and inhomogeneous illumination. Subsequent morphology analysis would benefit from high quality neuron images. In tracing algorithms [4, 5], all pixels with high intensity values are taken as possible components of neurons, and the tree structures are pruned as iteration goes. Starting with neuron images having clear backgrounds and high contrast, tracing methods like [4–6] not only converge quickly but also may result in more accurate neuron skeletons.

Unlike enhancement tasks for natural images, neuron image enhancement focuses on one class of objects, the neurons. Because of the varying content of natural images, enhancement algorithms for natural images usually take the approach of modeling natural scene statistics [7, 8]. In contrast, there are two unique properties for neuron images, the gradient sparsity and the tubular structure. We hypothesize that the exploitation of these two priors is the key to achieving satisfactory results for neuron image enhancement. Most existing neuron image enhancement methods make use of the property of tubular structure with two categories of approaches. The first category of approaches, such as [9–11], measures the prominence of tubular structures with eigenvalues derived from local gradients. The second category of approaches, such as [12–15], uses multi-direction and multi-scale filters. By selecting the maximum response of different filters at each pixel, pixels belong to tubular structures are augmented. However, by not accounting for the gradient sparsity, these methods lead to unwanted enhancement of faint clutter or false removal of neuron joints. The second column in Fig. 1 demonstrates these two situations. Another innate drawback of existing neuron enhancement methods is that the neuron intensity distribution is altered and details are erased. Such an intensity distribution is an important clue for classification of neuron phenotype and neuron activity monitoring, for example [16].

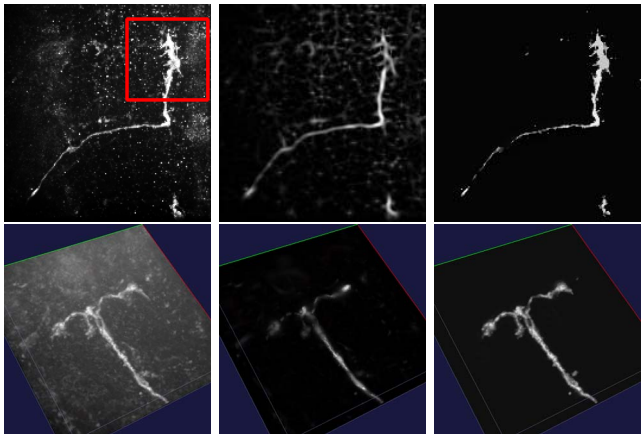

Fig. 1: The first column are original neuron images. The second column are enhanced results by LDE [12] for the 2D image (N1), and by Frangi's method [9] for the 3D image (M1). The third column are enhanced results of the proposed CaNE.

In this paper, we propose a novel content-aware neuron enhancement (CaNE) method that includes both priors of the gradient sparsity and the tubular structure. In CaNE, neuron enhancement is formulated as an optimization problem with cost terms of the data fidelity and the structure weighted gradient sparsity. Experiments on both 2D and 3D neuron images show that CaNE is effective at removing artifacts while preserving details in neurons. With enhanced images by CaNE, segmentation and tracing algorithms can get more accurate results.

This paper is organized as follows. Section 2 introduces priors of gradient sparsity and tubular structure in neuron im-

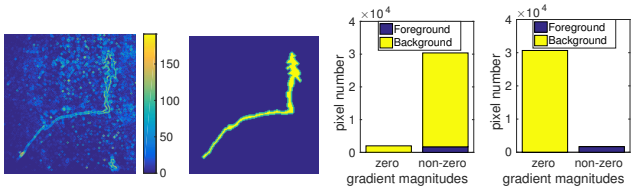

(a) (b) (c) (d)

Fig. 2: (a) Gradient magnitudes of N1 shown in Fig. 1. (b) The manually segmented neuron mask. Boundaries in green are counted as foreground. (c) The distribution of (a). (d) The gradient magnitude distribution with the mask in (b).

ages. Section 3 elaborates on the implementation of the proposed CaNE and illustrates the functionality of each prior. Section 4 compares CaNE with other neuron enhancement methods, and verifies advantages of artifact removal and detail preserving of CaNE. Finally, novelty and limitations of the proposed method and future work are discussed in Section 5.

2. PRIORS FOR NEURAL IMAGING

As reviewed in Section 1, two important priors of neuron images are the gradient sparsity and the tubular structure. In this section, we discuss these two priors separately and select corresponding models.

2.1. Gradient Sparsity

The gradient distribution is used as prior information in many image restoration tasks. A trade off is achieved between the data fidelity and the gradient sparsity for signal denoising, deblurring or smoothing [17–19].

Ideal neuron images should have constant backgrounds. However, most non-zero gradient magnitudes are caused by noise and clutter in the background. Fig. 2(a) and (c) show gradient magnitudes of image N1. By enforcing a constant background with the mask in Fig. 2(b), the gradient magnitude distribution of an ideal neuron image is shown in Fig. 2(d). Therefore, the gradient sparsity is an effective assumption to obtain clear backgrounds in neuron images.

Assuming I is the original image and S is the enhanced image, the enhancement task considering the gradient sparsity can be formulated as,

$$S = \underset{S}{\operatorname{argmin}} \|S - I\|_i + \lambda \cdot \|\nabla S\|_0. \tag{1}$$

Common choices of i are 0, 1 and 2. For many image restoration methods [17, 19, 20], i is set as 2 because the L2 norm is differentiable. However, in neuron images, faint clutter and inhomogeneous illumination are two major artifacts. L1 or L2 norm of data fidelity tends to create layering artifacts or retain the inhomogeneous illumination. The proposed CaNE adopts L0 norm for the data fidelity term. More discussion about the choice of i and results are in Section 3.

2.2. Tubular Structure

Though the gradient sparsity is effective at removing clutter, the tubular structure prior of neurons is not used. As a result, noise with high intensity cannot be differentiated from neurons. Though existing neuron enhancement methods propose several ways to measure the tubular structure [6, 9, 12], we find the image content index [21], Q, is robust to capture the tubular structure. The original Q used for image quality assessment [21], is defined as,

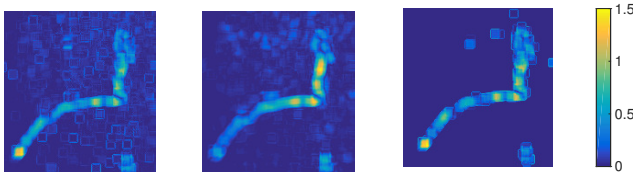

Fig. 3: The tubular structure prominence [21], Q, for the images in the first row of Fig. 1.

$$Q = s_1 \cdot \frac{s_1 - s_2}{s_1 + s_2},$$

where s_1 and s_2 are the singular values of local gradient matrices and $s_1 \geq s_2$. For 3D images, there are three singular values for each local gradient matrix. Because two large and one small singular values characterize 3D tubular structures [14], we calculate Q as,

$$Q = s_1 \cdot s_2 \cdot \frac{s_1 - s_3}{s_1 + s_3}, s_1 \geq s_2 \geq s_3.$$

3. CONTENT-AWARE IMPLEMENTATION

Once having math models of two priors, the neuron enhancement is formulated as,

$$S = \underset{S}{\operatorname{argmin}} \|S - I\|_0 + \lambda \cdot \sum_p \frac{1}{Q(p)} \|\nabla S(p)\|_0. \tag{2}$$

As in Section 2, I represents the original image, S represents the enhanced image, and Q is the structure prominence index [22]. Compared with Eqn. 1, Eqn. 2 relaxes the gradient sparsity constrain by $\frac{1}{Q}$ where tubular structures exist. In order to solve Eqn. 2 efficiently, we introduce two auxiliary variables, $d = S - I$ and $u = \nabla S$. Then the problem in Eqn. 2 becomes,

$$\min_{S,d,u} \|d\|_0 + \sum_p \frac{\lambda}{Q(p)} \|u(p)\|_0 + \eta \|S - I - d\|_2^2 + \beta \|\nabla S - u\|_2^2. \tag{3}$$

Eqn. 3 can be further broken into three sub-problems according to each variable,

$$\min_S \|S - I - d\|_2^2 + \frac{\beta}{\eta} \|\nabla S - u\|_2^2, \tag{4}$$

$$\min_u \|\nabla S - u\|_2^2 + \sum_p \frac{\lambda}{\beta \cdot Q(p)} \|u(p)\|_0, \tag{5}$$

$$\min_d \|d\|_0 + \eta \|S - I - d\|_2^2. \tag{6}$$

Alg. 1 provides solutions to three sub-problems and summarizes key steps of the proposed CaNE. In Alg. 1, gradient u is broken into two parts for clarity, the horizontal gradient h and the vertical gradient v, and D_x and D_y are two corresponding difference matrices. In order to get a robust and

Algorithm 1 Solution to Eqn. 2

Initialization;

$d = 0$ ▷ $S = I$

while not convergence **do**

1. Calculate the tubular structure index Q of S
2. $S \leftarrow \frac{\eta(I+d)+\beta D_x^T h+\beta D_y^T v}{\eta+\beta D_x^T D_x+\beta D_y^T D_y}$ ▷ Eqn. 4
3. $h \leftarrow D_x S$, $v \leftarrow D_y S$
4. if $h(p)^2 + v(p)^2 > \frac{\lambda}{\beta \cdot Q(p)}$, $h(p) \leftarrow 0, v(p) \leftarrow 0$ ▷ Eqn. 5
5. $d \leftarrow S - I$
6. if $d(p)^2 > \frac{1}{\gamma}, d(p) \leftarrow 0$ ▷ Eqn. 6
7. $\beta \leftarrow \kappa \cdot \beta, \eta \leftarrow \kappa \cdot \eta$

end while

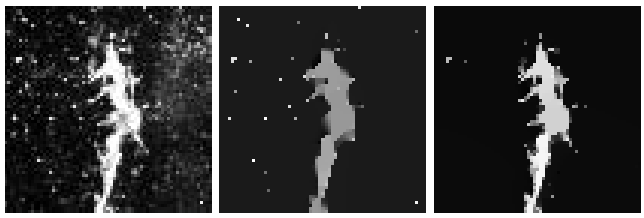

(a) (b) (c)

Fig. 4: (a) is the highlighted patch in Fig. 1. (b) and (c) are enhanced results without and with the structure prior.

accurate solution to Eqn. 2, β and η keep increasing at the rate κ to enforce equality constrains for two auxiliary variables.

Fig. 4 illustrates the effect of the tubular structure prior in CaNE. Without this structure prior, noise with high intensity cannot be removed even when the neuron structure blurs as shown in Fig. 4(b). In Fig. 4(c), a better trade off between noise removal and neuron structure preservation is achieved by adjusting the gradient sparsity weight according to the tubular structure index.

If the data fidelity term in Eqn. 2 is calculated by L2 norm, the enhancement task can be solved similarly, but the auxiliary variable d is not needed anymore because the L2 norm is differentiable. Fig. 5 compares data fidelity terms with L2 and L0 norms. Neuron structures in Fig. 5(b) start to blur, while cloudy artifacts still exist. The enhanced result in Fig. 5(c) has a clearer background and preserves neuron structures better. The explanation to this result is that the data fidelity term in L2 norm always tries to constrain the enhanced pixel values to the original ones. However, the data fidelity term in L0 norm stops adding extra penalty to pixel value adjustment once original values are changed. As a result, the gradient sparsity term dominates the evolution in background areas for L0 case.

4. EXPERIMENTS

Alg. 1 has four parameters, λ, β, η and κ. The smoothness of the enhanced image is mainly controlled by λ. The other three parameters, β , η and κ, are introduced to guarantee a numerically stable solution. In all our experiments, β is initialized as λ, η is initialized as 2000λ, and the increasing rate κ is set as 2. The iteration number is set as 30. Only the variable λ is manually selected to ensure a balance between clear backgrounds and neuron detail preservation. In next two parts, we test CaNE with 2D and 3D neuron images and demonstrate how CaNE facilitates the neuron segmentation and skeleton detection.

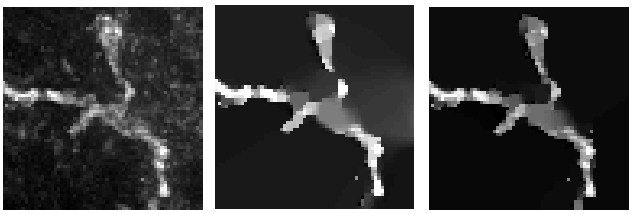

(a) (b) (c)

Fig. 5: (a) is the highlighted patch in Fig. 6(c). (b) and (c) are enhanced results with data fidelity terms of L2 norm and L0 norm respectively.

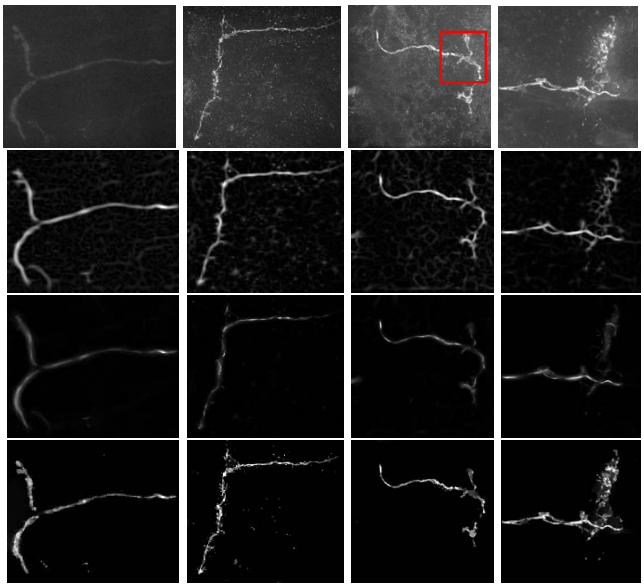

(a) (b) (c) (d)

Fig. 6: The first row are the original neuron images [23], N2-N5. N1 is shown in Fig. 1. The second row to the fourth row are the enhanced results by LDE [12], Frangi's method [9] and CaNE respectively.

4.1. 2D Enhancement

Two other neuron enhancement methods, LDE [12] and Frangi's method [9], are compared with CaNE. Five 2D neuron images [23], N1-N5, are tested in this part.

In Fig. 6, LDE creates phantom structures in the background. Frangi's method gets clearer backgrounds but also suppresses the visibility of the neuron structure. Both LDE and Frangi's method alter the intensity distribution within neurons and this may cause difficulty for neuron classification [2] and activity monitoring [16]. CaNE removes most

Table 1: Neuron enhancement for 2D images

		N1	N2	N3	N4	N5	**Ave**
Dice	Frangi	0.6591	0.7912	0.6059	0.6438	0.3196	0.6039
	LDE	0.6118	0.8371	0.7764	0.7970	0.6381	0.7321
	CaNE	0.7076	0.8635	0.7457	0.8252	0.7171	**0.7718**
Corr	Frangi	0.7374	0.6960	0.7085	0.7026	0.6975	0.7084
	LDE	0.6948	0.7093	0.6959	0.7071	0.7553	0.7125
	CaNE	0.9631	0.9717	0.9671	0.9114	0.9649	**0.9556**

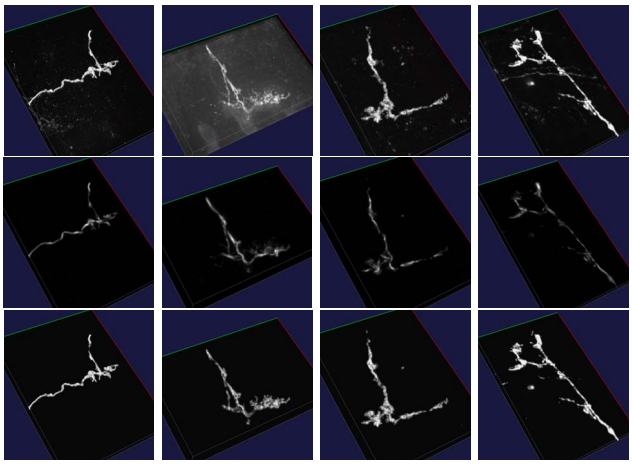

Fig. 7: The first row are the original neuron images also used in [6], M2-M5. M1 is shown in Fig. 1. The second row and the third row are the enhanced results by Frangi [9] and CaNE respectively.

artifacts and preserves the intensity distribution in neurons.

Table 1 provides quantitative results of different enhancement methods. The Dice index evaluates the accuracy of binary segmentation [24] after different enhancement methods. The Dice index is defined as, $D = \frac{2|s_t \cap s_g|}{|s_t|+|s_g|}$. Here s_g denotes the ground truth segmentation and s_t is the result of an automated method. The Dice index is within $[0, 1]$. A larger Dice index means a more accurate segmentation result. In order to measure the detail preservation of different enhancement methods, we use the correlation between the original image and the enhanced result within the neuron area. A higher correlation indicates the enhanced neuron image has higher data fidelity with the original data. The proposed CaNE yields the best performance under both criteria, and notably so in the case of the correlation.

4.2. 3D Enhancement

Since LDE does not have a 3D implementation, CaNE is compared with the widely-used Frangi's method in this part. The 3D neuron images, M1-M5, are from [6].

Fig. 7 shows the enhanced results by the Frangi's method and CaNE. Though both methods remove artifacts well, CaNE preserves details better and provides higher contrast. Because the ground truth for 3D neuron images only have the skeleton information, a skeleton extraction method [25] is used to obtain neuron skeletons from the enhanced results. Fig. 8 shows the skeletons of M1 (shown in Fig. 1). The detected skeleton from the enhanced image by Frangi's method [9] is not consistent and misses some end branches.

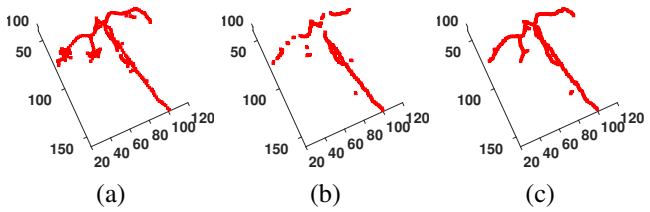

Fig. 8: (a) The skeleton ground truth of M1 (shown in Fig. 1). (b)-(c) Extracted skeletons with enhanced images by Frangi's method and CaNE.

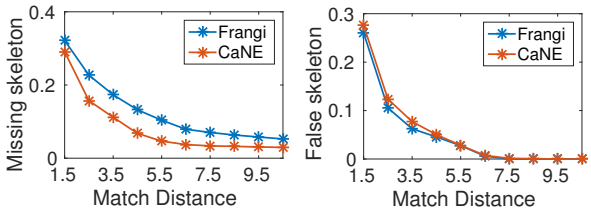

Fig. 9: Average missing percentage and surplus percentage of five 3D neuron images.

Different from the Dice index for 2D segmentation, the accuracy measurement of skeleton detection should be evaluated on different tolerance distances. Missing percentage at the tolerance distance i is defined as, $M_{per}(i) = \frac{\#min\_dist(s_g,s_t)>i}{\#s_g}$. Here s_g is the skeleton ground truth, s_t is the detected skeleton, and $min\_dist(s_g, s_t)$ is the minimum distance for a point in s_g to all the points in s_t. $M_{per}(i)$ measures the percentage of the skeleton ground truth that does not have a corresponding point in the detected skeleton within range i. Similarly, surplus percentage, $S_{per}(i)$, measures the percentage of the detected skeleton that does not have a corresponding point from the skeleton ground truth within range i. Surplus percentage is defined as, $S_{per}(i) = \frac{\#min\_dist(s_t,s_g)>i}{\#s_t}$. Fig. 9 shows the average missing percentage and surplus percentage. Skeletons detected based on CaNE have better performance in terms of missing percentage than those based on Frangi's method. Frangi's method is slightly better in terms of surplus percentage when the tolerance range is small, but this may not reflect performance difference at features of interest such as at bifurcations and complex structures found at neuron termini.

5. CONCLUSIONS

We proposed a novel neuron image enhancement method that exploits the gradient sparsity and the tubular structure priors for neuron images. The contributions of this method are twofold. First, two important priors of neuron images are combined into one cost function. Second, an effective solution is provided to get the enhanced neuron image.

Further work will verify CaNE on a larger dataset such as provided in the BigNeuron [1] initiative and test the algorithm on other filamentous images, such as retina images. In addition, we plan to fully automate the enhancement process with smoothing parameter selection [22].

6. REFERENCES

[1] H. Peng et al., "BigNeuron: large-scale 3D neuron reconstruction from optical microscopy images," *Neuron*, vol. 87, no. 2, pp. 252–256, Jul. 2015.

[2] K. Rajkovic et al., "Mathematical modeling of the neuron morphology using two dimensional images," *Journal of Theoretical Biology*, vol. 390, pp. 80–85, 2016.

[3] Z. Li et al., "Indexing and mining large-scale neuron databases using maximum inner product search," *Pattern Recognition*, vol. 63, pp. 680–688, 2017.

[4] H. Peng, F. Long, and G. Myers, "Automatic 3D neuron tracing using all-path pruning," *Bioinformatics*, vol. 27, pp. i239–i247, 2011.

[5] H. Xiao and H. Peng, "APP2: automatic tracing of 3D neuron morphology based on hierarchical pruning of a gray-weighted image distance-tree," *Bioimage informatics*, vol. 29, no. 11, pp. 1448–1454, 2013.

[6] S. Mukherjee, B. Condron, and S. T. Acton, "Tubularity flow field– a technique for automatic neuron segmentation," *IEEE Trans. on Image Processing*, vol. 24, no. 1, pp. 374–390, Jan. 2015.

[7] P. Chatterjee and P. Milanfar, "Is denoising dead?," *IEEE Trans. on Image Processing*, vol. 19, no. 4, pp. 895–911, 2010.

[8] D. Krishnan and R. Fergus, "Fast image deconvolution using hyper-laplacian priors," in *NIPS*, 2009, pp. 1033–1041.

[9] A. F. Frangi et al., "Multiscale vessel enhancement filtering," in *MICCAI*, 1998, pp. 130–137.

[10] R. Manniesing et al., "Vessel enhancing diffusion: A scale space representation of vessel structures," *Medical Image Analysis*, vol. 10, no. 6, pp. 815–825, 2006.

[11] T. Kohler et al., "Automatic no-reference quality assessment for retinal fundus images using vessel segmentation," in *Computer-Based Medical Systems*. IEEE, 2013, pp. 95–100.

[12] S. Mukherjee and S. T. Acton, "Oriented filters for vessel contrast enhancement with local directional evidence," in *International Symposium on Biomedical Imaging*, 2015, pp. 503–506.

[13] K. Krissian et al., "Model-based detection of tubular structures in 3D images," *Computer Vision and Image Understanding*, vol. 80, no. 2, pp. 130–171, 2000.

[14] S. Basu, B. Condron, A. Aksel, and S. T. Acton, "Segmentation and tracing of single neurons from 3D confocal microscope images," *IEEE J. Biomedical and Health Informatics*, vol. 17, no. 2, pp. 319–335, 2013.

[15] M. Sofka and C. V. Stewart, "Retinal vessel centerline extraction using multiscale matched filters, confidence and edge measures," *IEEE Trans. on Med. Imag.*, vol. 25, no. 12, pp. 1531–1546, 2006.

[16] L. B. Cohen, B. M. Salzberg, and A. Grinvald, "Optical methods for monitoring neuron activity," *Annual review of neuroscience*, vol. 1, no. 1, pp. 171–182, 1978.

[17] L. Condat, "A direct algorithm for 1-D total variation denoising," *IEEE Signal Processing Letter*, vol. 20, no. 11, pp. 1054–1057, 2013.

[18] T. Dai, C. Song, J. Zhang, and S. Xia, "PMPA: a patch-based multiscale products algorithm for image denoising," in *ICIP*. IEEE, 2015, pp. 4406–4410.

[19] L. Xu, C. Lu, Y. X, and J. Jia, "Image smoothing via L_0 gradient minimization," *ACM Transactions on Graphics*, vol. 30, no. 6, pp. 174–186, Dec. 2011.

[20] T. Goldstein and S. Osher, "The split bregman method for L1-regularized problems," *SIAM J. Imaging Sciences*, vol. 2, no. 2, pp. 323–343, 2009.

[21] X. Zhu and P. Milanfar, "Automatic parameter selection for denoising algorithms using a no-reference measure of image content," *IEEE Trans. on Image Processing*, vol. 19, no. 12, pp. 3116–3132, Dec. 2010.

[22] H. Liang and D. S. Weller, "Comparison-based image quality assessment for selecting image restoration parameters," *IEEE Trans. on Image Processing*, vol. 25, no. 11, pp. 5118–5130, Nov. 2016.

[23] R. Sarkar, S. Mukherjee, and S. T. Acton, "Dictionary learning level set," in *Signal Processing Letters*. IEEE, 2015, pp. 2034–2038.

[24] N. Otsu, "A threshold selection method from gray-level histograms," *IEEE Trans. on Systems, Man, and Cybernetics*, vol. 9, no. 1, pp. 62–66, 1979.

[25] T. Lee, R. L. Kashyap, and C. Chu, "Building skeleton models via 3-D medial surface/axis thinning algorithms," *Computer Vision, Graphics, and Image Processing*, vol. 56, no. 6, pp. 462–478, 1994.